Nuclear Materials Authority
P.O.Box 530 Maadi, Cairo, Egypt

GEOCHEMICAL CHARACTERISTICS AND RADIOACTIVE POTENTIALITY OF SOME METAMORPHIC ROCKS IN WADI SIKAIT, SOUTHEASTERN DESERT, EGYPT

MOUSTAFA E. GHARIEB, MOHAMED E. IBRAHIM[1], GAMAL EL-DEEN M. ATTIA, SAMEH H. NEGM[1], HOSSAM E. ABU-ELMAATI[1] and TAREK F. MOHAMMADEN[1]

Dept. Geol.,, Fac. Sciences, Helwan Univ., Egypt; [1] Nuclear Materials Authority, Cairo,Egypt

ABSTRACT

Sikait area locates between Lat. 24° 37' 16" to 24° 38' N and Long. 34° 46' to 34° 46' 35" E. It comprises several igneous and metamorphic rocks which mainly dissected by lamprophyre dykes and quartz veins. From the radioactivity point of view, the metamorphosed sandstone and the mylonite rocks were selected for this work. The petrographical features indicated that the metamorphosed sandstone is of greywacke type and probably sourced from igneous and metamorphic rocks while the mylonite was belonging to the granitic rocks. On the other hand the metamorphosed sandstone was found as pssamitic greywacke affected by albitiztion process and both the island arc and the felsic igneous are its tectonic environment and provenance respectively. The mylonite exhibited calc-alkaline and peralumenous nature of A-type granite that emplaced in the within-plate environment and affected by Na-metasomatism. The radiometric characteristics revealed a disequilibrium phase in both the rocks due to uranium addition process that play an important role in deposition of recent uranium and formation of the secondary uranium minerals particularly in the mylonite, while uranium in the metamorphosed sandstone is probably absorbed as free element on the clay matrix. Both the rocks are regarded as promising sources for the uranium exploitation.

INTRODUCTION

The metamorphosed rocks at Nugrus–Sikait District, are mainly exposed in two nappes; the upper nappe (dismembered ophiolitic rocks) and lower nappe (pelitic, para-amphibolite and cataclastics assemblages) separated by ophiolitic mélange and it is believed that the area was subjected to five distinct episodes of deformation (Ibrahim et al., 2014). Also, the same workers pointed to that the tectonic evolution of the Nugrus-Sikait belt (NSB) can place important insights into a proposed tectonic model suggesting a back-arc basin tectonic environment.

The cataclastic rocks in Nugrus-Sikait belt show a unique fish-shaped exposure and its protolith is a highly differentiated batholith formed of porphyry biotite granite in the north (at the upper stream of Wadi Sikait) followed southward by biotite granite and two-mica granite (Khaleal, 2005).

The exposed rocks in Wadi Sikait were

distinguished into three domains; the ophiolitic, cataclastic rocks and intrusive domains with a main mineralized shear zone at the contact between the cataclastic rocks and the overlying ophiolitic rocks (Khaleal et al., 2007 and Saleh et al., 2012). Also, these cataclastic rocks are rich in several types of the mineralization including the base metals and accessory phases (Ibrahim et al., 2015).

The psammitic gneisses in Wadi Sikait was considered as foliated granites derived by cataclasis from granitic rocks of calc-alkaline to per-alkaline nature and the hornblende gneisses as intrusive dioritic represent the plutonic equivalent of the calc-alkaline volcanic rocks cataclasis (Ries et al., 1983 and Hegazy, 1984).

The origin of metamorphosed sandstone rocks in Sikait area is believed to be the sandstones which have been subjected to heat with or without pressure and they are consists of recrystallized and tightly interlocking grains of quartz and outcropped at two locations and intruded by fertile porphyritic granite and lamprophyre dykes.

The Sikait area was traversed by several dykes, particularly the lamprophyre dykes, and veins of different composition trending NW-SE and NE-SW (Ibrahim et al., 1999). The Sikait lamprophyre dykes are considered barren in mineralization compared with Abu Rusheid lamprophyres (Ibrahim and Ragab 2011 and Ibrahim et al., 2015).

The radioactive mineralization in Sikait area was regarded to be originated as a result for the re-crystallization of the whole rocks which took place during the metamorphism processes (Hassan 1964 and 1973).

The current study concerns with mylonitic rocks and the metamorphosed sandstone due to their elevated potentiality from the radioactivity point of view comparing to the other encountered rock units in Sikait area. Their petrographical, geochemical and radioactive characteristics will be the scope of this study.

GEOLOGIC SETTING AND PETROGRAPHY

Wadi Sikait locates between Lat. 24° 37' 16" to 24° 38' N and Long. 34° 46' to 34° 46' 35" E and strikes WNW-ESE. It can be easily accessed from the Red Sea coast through Wadi El-Gemal then Wadi Nugrus along a desertic track of about 49 km long. The area is characterized by arid to semi-arid weather and scarcity of the water resources.

The main rock units exposed in Wadi Sikait area include; the ophiolitic mélange, metamorphosed sandstone and porphyritic biotite granite as well as small gabbroic bodies (Fig. 1), while the cataclastic rocks (mylonite) are exposed more northern along Wadi Sikait in addition to other rock varieties (Fig. 2)

The ophiolitic mélange are mainly confined to the eastern side of Wadi Sikait area. It is characterized by medium-grained size and greyish green color with mafic-ultramafic mixed fragments and blocks embedded in fine to coarse-grained metasedimentary matrix (Ibrahim et al., 2010, Saleh et al., 2012 and Ibrahim et al., 2014).

The mylonites exposed in the central part of eastern sector along Wadi Sikait and cover an area of about 0.8 km^2 with an average elevation about 5m above Wadi Sikait alluvium and affected by two sets of strike-slip faults (NNW- SSE right lateral and N-S left lateral). Mylonites are mostly fine to medium grained and comprise quartz veins outcome from the extensive recrystallization and remobilization of quartz. The main alterations are represented by hematitization, silicification, greisenization, fluoritization, albitization and pyritization.

The porphyritic biotite granites occupy the western sector of Wadi Sikait area and characterized by intensive shearing, sharp contacts with the older rocks, gneissosity structure and engulf elongated xenoliths of metamorphosed sandstone and mafic rocks. Their textural features indicate that subsolidus plastic deforma-
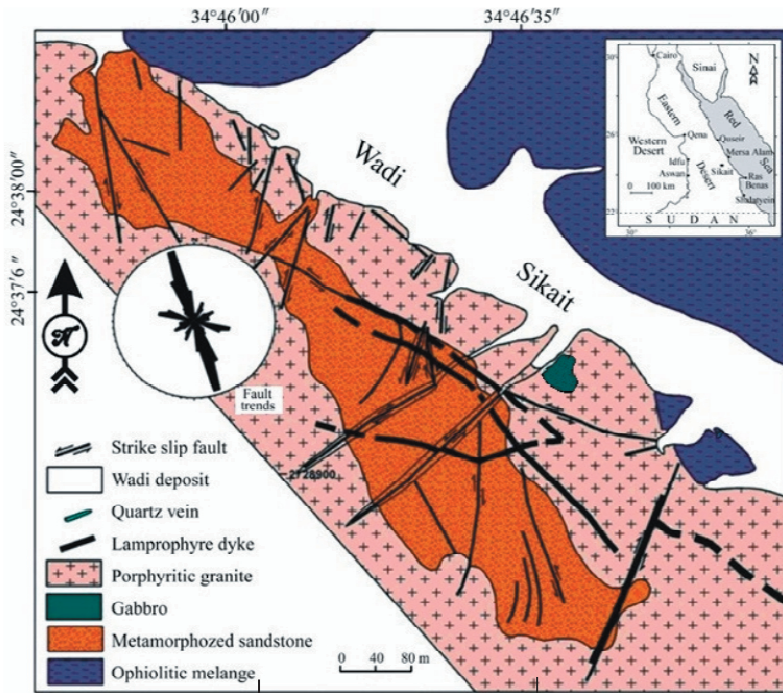
Fig. 1: Geologic map of Wadi Sikait shows the exposed metamorphosed sandstone, (After Ibrahim et al., 2010)
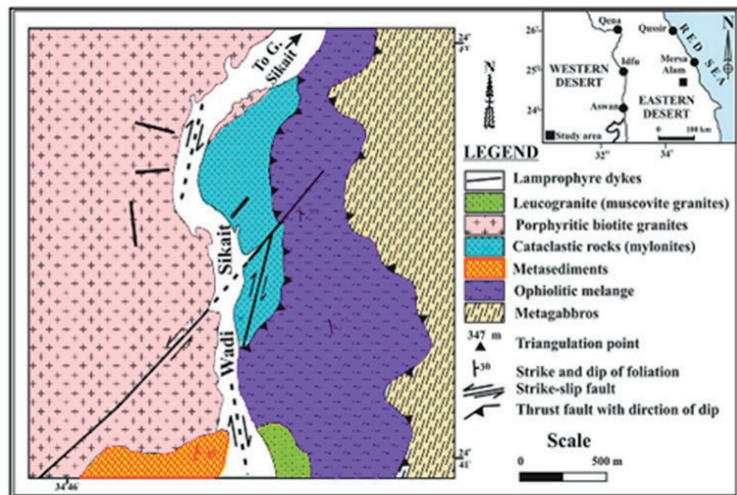

Fig. 2: Geologic map of Wadi Sikait shows the exposed mylonite, (After Saleh, 1997)

tion was induced during the extensive thrusting (Mohamed and Hassanen, 1997 and Saleh et al., 2012). They are dissected bylamprophyre dikes (strike N50º W-S 50º E and dips 65º due NE) as well as strongly deformed and brecciated barren quartz veins (Ibrahim et al,.2010 and Saleh et al., 2012).

The metamorphosed sandstone rocks are fine-grained, white in color, highly sheared, banded, less foliated and cross-cut by lamprophyre dykes (NW-SE, N-S, and E-W) and quartz veins (NNW-SSE, NNE–SSW and E-W). The metamorphosed sandstone rocks are cut by the lamprophyre dykes as well as several sets of strike-slip faults and one set of dip-slip fault that form a good fracture system acts as relevant pathwyas for the solutions (Ibrahim et al., 2010). The weathered surface has a granular appearance with common vugs filled with secondary mineralization while the common alteration products are represented by hematitization and manganese dendrites

The gabbros cover a limited small area (20 -30m) and occur as high hills in the eastern sector of Wadi Sikait area (Saleh, 1997). The rocks are fine to medium-grained, dark grey in color and intruded by the porphyritic granites and usually characterized by presence of dark green hornblende and absence of layering and lamination.

Several lamprophyre dykes and quartz veins cut into the metamorphosed sandstone and the porphyritic granites. The lamprophyre dykesare fine to medium-grained, sheared, black grey in color, discontinuous and vary in thickness and length while their altered parts are generally considered as good traps for mineralization (Ibrahim et al., 2007). On the other hand, the quartz veins are represented by two generations; the first represented by the barren quartz veins that cross-cut the foliation planes of metamorphosed sandstone and the second is the mineralized quartz veins which bear visible mineralization and parallel to the foliation planes.

Petrographical Features of the Metamorphosed Sandstone

Petrographically, the metamorphosed sandstone is represented mainly by quartz and less amount of k-feldspars, plagioclase and micas. The constituent grains are of extreme variable size reflecting the poorly sorted nature of the metamorphosed sandstone (Fig. 3) and they embedded in a fine-grain matrix which is most probably clay grains. This matrix forms a major constituent and exceeds 15% of the rock composition indicateing that the studied metamorphosed sandstone is a greywacke type (Fig. 4). The high matrix ratio as well as the poorly sorting and the subrounded to sub-

Fig. 3: Photomicrograph shows Poorly-sorted grains and polycrystalline quartz with sutured boundaries, XPL

Fig. 4: Photomicrograph shows greywacke with matrix exceeds 15% and sandstone rock fragment, XPL

angular shapes of the components, point to the textural immaturity of the studied rock.

The quartz grains are mainly monocrystalline and occasionally polycrystalline with subrounded to subangular shapes. The boundaries between quartz grains sometimes exhibit the straight or sutured forms (Fig. 5) which suggests the igneous and metamorphic source of these grains. Generally, the quartz grains exhibit faint to moderate unduloseextinction which may reflect that the studied rock would not subject to high stresses after its deposition.The rock fragments appeared as sandstone fragments (Fig. 4). The cement materials are probably clay grains and very fine quartz grains, also the calcite cement was observed as filling materials between the grains boundaries .

The K-feldspar is represented by the microcline which easily identified by its cross-hatched twinning (Fig. 6). The plagioclase grains usually exhibit the albite twinning but some grains showed a combination between the Carlsbad and albite twinning (Fig. 7). It the worth to mention that both the K-feldspars and plagioclase show no signs of alteration and appeared as fresh grains supporting that the studied metamorphosed sandstone was driven by mechanical weathering rather than the chemical weathering. The preserved lamella of plagioclase without distortion supports that the rock did not subject to high-magnitude stresses.

Micas are represented by small muscovite flakes embedded in the matrix materials . Presence of muscovite and absence of biotite grains may be encouraged the granitic source of metamorphosed sandstone.

Petrographical Features of the Mylonite

The investigated mylonitic rocks are composed of, in descending order, quartz, K-feldspars, plagioclase and micas reflecting their granitic composition with rare alteration features. Zircon and xenotime are the commonly observed accessory minerals while the

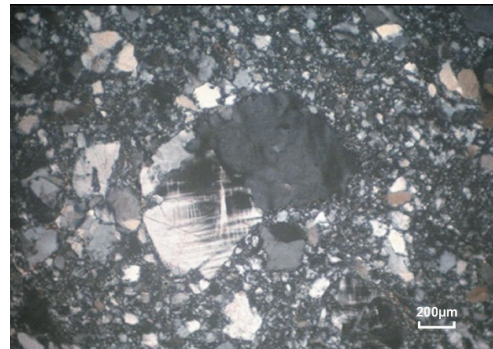Fig. 5: Photomicrograph shows monocrystalline Qz-grains and polycrstalline Qz of straight boundaries, XPL

Fig. 6: Photomicrograph shows anhedral microcline showing the cross-hatch twining embedded into matrix materials and corroded, XPL

Fig. 7: Photomicrograph shows anhedral to subhedral Qz-grains and brocken albite-twinned plagioclase, XPL

radioactive minerals were represented in the uranophane and probably the kasolite.

The quartz crystals appeared to be crystallized in three phases or may be more. The most recent phase represented by quartz grains free from the extinction feature that neans they did not subject to stress after their crystallization (Fig. 8). The second phase is indicated by those quartz grains of faint to wavy extinction reflecting light to moderate stress (Fig. 9) while the oldest phase is represented by quartz grains of high undulatory extinction and suffered from strong dynamic stresses supported by their stretching, elongation and moreover their fragmentation (Fig. 10). The undulose extinction is probably attributed to creation of defects, notably dislocation in the lattice when crystal is deformed or strained due to increaseing of the free energy of the crystal (Yardly, 1989).

The K-feldspar usually represented by orthoclase perthite of coarse to medium and subhedral crystals of string type perthite. Some perthites engulfed inclusions of quartz grains in a poikilitic form (Fig. 11) while some are corroded by other quartz-grains indicating the polyphase of crystallization. Sometimes an exsolvation of plagioclase can be noticed at the rims of the orthoclase perthite where the plagioclase crystals show an optical continuity with its hosting K-feldspar (Fig. 12). Approximately, all the perthite crystals are fresh where no signs of alteration were observed. The microcline perthite with the characteristic cross-hatching twinning was identified but in a lesser amount than the orthoclase perthite (Fig. 13). Also, the non-perthitic orthoclase was observed as subhedral medium crystals of printed ends revealing the Carlsbad twinning (Fig. 14).

The plagioclases are of anhedral shape and medium to small sized crystals. They are mostly within the oligoclase composition range (An_{13-18}). Although the effect of deformation and the lamellae undulation, the plagioclase crystals are twinned according to the albite law and sometimes show the manebach
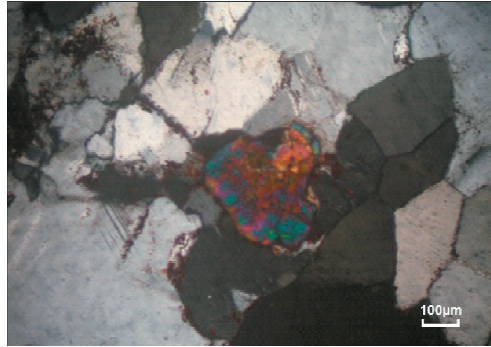

Fig. 8: Photomicrograph shows angular to sub-angular Qz crystals free from the extinction feature and xenotim crystal, XPL
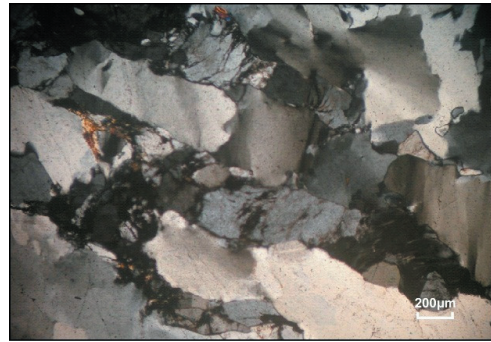

Fig. 9: Photomicrograph shows anhedral Qz crystals show faint to moderate undulose extinction, XPL

Fig. 10: Photomicrograph shows highly deformed Qz crystals as well as fragmented grains due to the high applied stresses, XPL
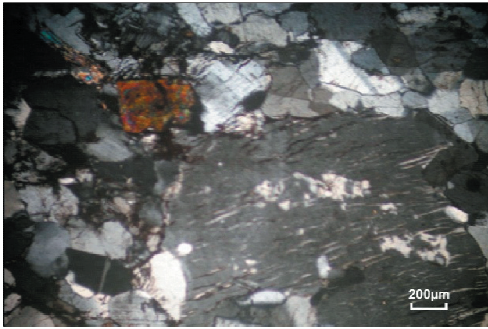
Fig. 11: Photomicrograph shows perthite crystal of string type engulfed Qz grains in a poikilitic form with subhedral xenotime crystal, XPL
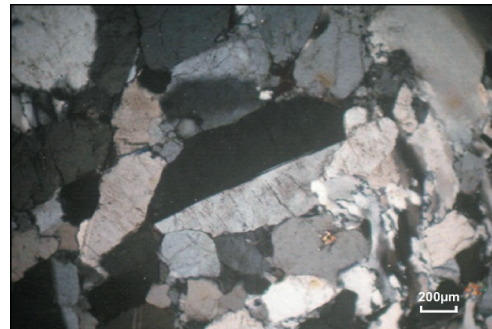

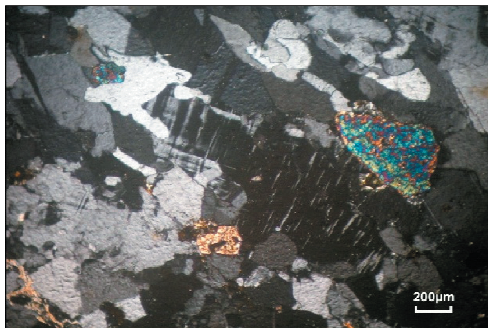Fig. 14: Photomicrograph shows subhedral orthoclase showing carlsbad twinnig, XPL

Fig. 12: Photomicrograph shows exsolved plagioclase showing albit lamellae at the upper corner of anhedral perthite with muscovite, XPL

twinning (Figs. 15&16). The traditional zoning of plagioclase crystals was not observed.

Muscovite is observed as interstitial small flakes between the major components (Fig. 12). The accessory minerals are represented by minute crystals of anhedral zircon of oval shape (Fig. 16) and xenotime as subhedral or anhedral crystals suffering some cracks and showing overgrowth (Figs. 8&11). The kasolite and uranophane, secondary uranium minerals, are easily identified in anhedral shaped and triangle shaped crystals respectively revealing high relief (Figs. 15&17).

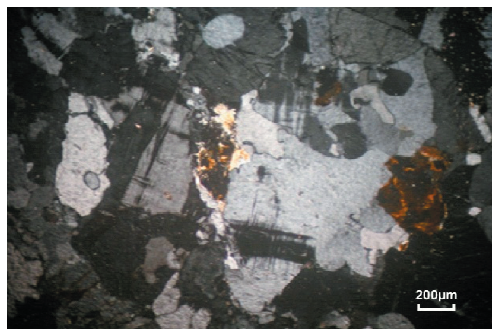Fig. 13: Photomicrograph shows microcline perthite with the tardional cross-hatching twinning, XPL

Fig. 15: Photomicrograph shows anhedral plagioclase of oligoclse composition showing manebach twining and kasolite crystals at the center and the right side, XPL

Fig. 16: Photomicrograph shows anhedral minute zircon crystal with plagioclase of deformed lamellae, XPL

Fig. 17: Photomicrograph shows subhedral uranophane, XPL

METHODOLOGY

The chemical and radiometric analyses were carried out at the laboratories of the Nuclear Materials Authority, (NMA).

The chemical analyses were carried out for the mostly fresh fourteen and thirteen samples from the mylonite and metamorphosed sandstone rocks respectively. The major elements, in the oxide form, were identified using the wet analytical methods after Shapiro (1975). The SiO_2, Al_2O_3, TiO_2 and P_2O_5 were determined by colorimetric spectrophotometer (LABOMED model SPECTRO UVD, USA), while the CaO, MgO and Fe_2O_3 were determined by the traditional titration technique and both Na_2O and K_2O were analyzed by the flame-photom-

eter (JENWAY model PFP7, UK). The identity and concentration of the trace elements were determined in the solid samples using the X-ray fluorescence (XRF, model PHILIPS X'Unique II) instrument under the conditions of W-target tube, LIF-220 crystal, gas flow proportional counter and scintillation counter 70 kV and 15 mA with detection limit 2 ppm. The analytical precision was ± 2% and ± 3% for the measured major and trace elements respectively.

The chemical concentration of U was measured using the UV/VIS spectrophotometer with the chemical reagent "Arsenazo III" according to the extraction method described by Marczenko (1986).

On the other hand, the radiometric concentrations of U, Th, Ra and K-40 were measured by the laboratory γ-spectrometry technique using the Multi-channel Gamma Spectrometer with NaI (Tl) detector. All the samples, after crushing to the relevant size, were carefully quartered and put into covered plastic vessels (212.6 cm^3 in volume) then tightly sealed by adhesive tapes. The sealed vessels were covered well by thin aluminum sheets to prevent escaping of the accumulated Ra-222 gas then were left for 30 days before the measuring process. Uranium, thorium (in their equivalent forms eU and eTh) and radium were measured and expressed in the ppm unit while K-40 concentration was in percentage.

THE GEOCHEMICAL CHARACTERISTICS AND SIGNATURES

The Metamorphosed Sandstone

Thirteen samples were analysed for their major and trace components and the obtained data are illustrated in Tables (1& 2).

•On the bi-variant diagrams of SiO_2 versus the other major oxides and trace elements (Figs.18-29), the scatter trend appears as common binary relations that may suggest the rock composition is mainly controlled by three mixing-component (quartz-illite-calcite) and

Table1: The major elements concentration (wt%) of metamorphosed sandstone, Sikait area

	SiO_2	Al_2O_3	TiO_2	Fe_2O_{3t}	MgO	CaO	K_2O	Na_2O	P_2O_5	L.O.I	Total %
S1	64.13	15.29	0.75	0.24	1.39	1.39	0.30	13.33	0.51	0.29	97.63
S2	63.81	15.22	0.08	0.23	1.39	1.39	0.27	13.28	0.50	0.29	96.46
S3	65.93	14.43	0.23	0.56	0.24	0.95	0.47	14.31	0.51	0.40	98.04
S4	64.77	16.15	0.07	0.16	0.32	0.84	0.33	14.31	0.39	0.75	98.11
S5	63.10	17.60	0.06	0.16	0.68	0.73	3.42	10.43	0.58	0.39	97.16
S6	62.40	16.76	0.00	0.64	0.52	0.90	3.68	11.37	1.10	0.76	98.13
S7	63.18	14.30	0.87	1.13	0.60	1.13	4.49	12.46	0.65	0.75	99.57
S8	64.17	15.47	0.95	1.29	0.60	0.73	3.68	11.37	0.81	0.54	99.61
S9	64.14	13.53	0.07	0.17	0.32	0.95	6.92	11.62	0.63	0.53	98.88
S10	64.83	16.71	0.64	0.72	0.36	0.84	2.51	11.79	0.32	0.42	99.15
S11	64.83	15.62	0.55	0.64	0.48	0.95	4.68	10.78	0.74	0.55	99.85
S12	66.57	15.47	0.86	1.21	0.60	0.95	0.31	12.88	0.85	0.19	99.90
S13	66.03	13.82	0.44	0.56	0.24	1.24	6.10	10.36	0.52	0.50	99.82
Min.	62.40	13.53	0.00	0.16	0.24	0.73	0.27	10.36	0.32	0.19	96.46
Max.	66.57	17.60	0.95	1.29	1.39	1.39	6.92	14.31	1.10	0.76	99.90
Aver.	64.45	15.41	0.43	0.59	0.60	1.00	2.86	12.18	0.63	0.49	98.64

Table 2: The trace elements concentration (ppm) of metamorphosed sandstone, Sikait area

	Cr	Ni	Cu	Zn	Zr	Rb	Y	Ba	Pb	Sr	Ga	V	Nb
S1	52.7	32.8	13.9	12.9	142.3	100.5	101.5	66.7	23.9	31.8	50.7	U.D	19.0
S2	52.5	32.6	13.9	12.9	139.7	100.1	100.9	66.0	23.8	31.6	50.2	U.D	25.0
S3	32.2	37.2	18.1	34.2	174.9	105.5	126.6	77.4	27.1	31.2	60.3	2.0	20.0
S4	58.3	30.2	14.1	16.1	420.1	102.5	110.6	125.6	18.1	41.2	105.5	3.0	24.0
S5	38.2	44.2	16.1	24.1	179.9	59.3	131.7	87.4	27.1	36.2	53.3	U.D	26.0
S6	24.1	46.2	12.1	24.1	431.1	39.2	113.6	120.6	19.1	39.2	101.5	2.0	23.0
S7	41.2	36.2	13.1	43.2	184.9	88.4	130.7	86.4	17.1	37.2	54.3	U.D	22.0
S8	14.1	49.2	24.1	15.1	450.2	61.3	188.9	143.7	23.1	41.2	102.5	2.0	17.0
S9	89.1	29.2	17.1	29.1	247.3	70.3	126.9	72.7	26.1	58.2	68.5	U.D	21.0
S10	38.2	34.2	16.1	32.2	150.8	39.2	105.5	62.3	17.1	29.1	55.3	U.D	19.0
S11	31.2	46.2	17.1	33.2	485.4	43.2	121.6	121.6	8.0	46.2	101.5	2.0	16.0
S12	55.3	49.2	16.1	33.2	425.1	116.6	123.6	61.3	24.1	34.2	96.5	U.D	11.0
S13	30.2	18.1	11.1	17.1	798.0	88.4	356.8	8.0	29.1	20.1	52.3	U.D	12.0
Min.	14.1	18.1	11.1	12.9	139.7	39.2	100.9	8.0	8.0	20.1	50.2	U.D	11.0
Max.	89.1	49.2	24.1	43.2	798.0	116.6	356.8	143.7	29.1	58.2	105.5	3.0	26.0
Aver.	42.9	37.4	15.6	25.2	325.4	78.0	141.4	84.6	21.8	36.7	73.3	1.8	19.6

Fig.18: Binary variation diagram of SiO_2 vs. Al_2O_3 for the metamorphosed sandstone

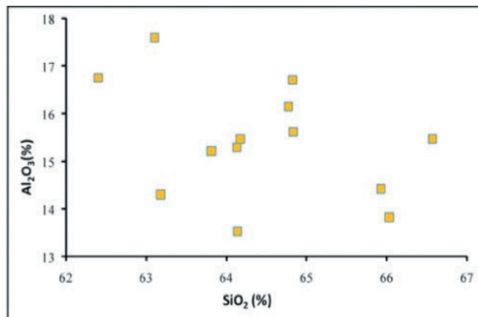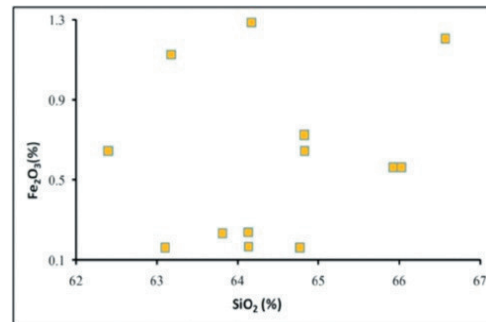Fig. 19: Binary variation diagram of SiO_2 vs. Fe_2O_3 for the metamorphosed sandstone
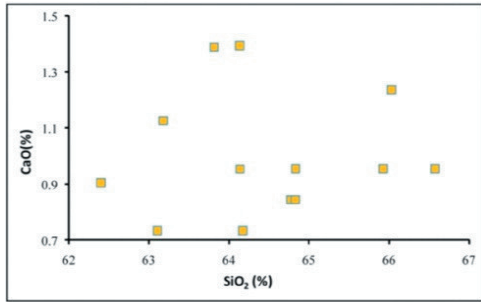
Fig. 20: Binary variation diagram of SiO$_2$ vs. CaO for the metamorphosed Sandstone

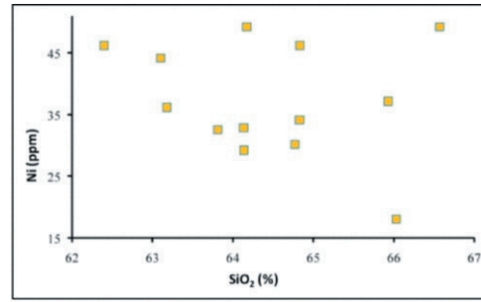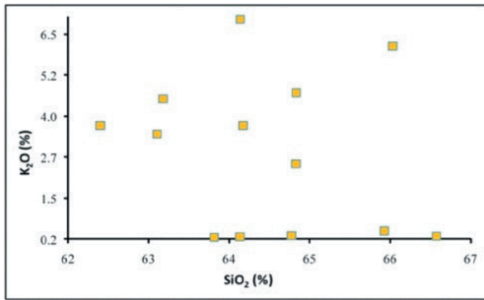Fig. 23: Binary variation diagram of SiO$_2$ vs. Ni for the metamorphosed sandstone

Fig. 21: Binary variation diagram of K$_2$O vs. Al$_2$O$_3$ for the metamorphosed sandstone
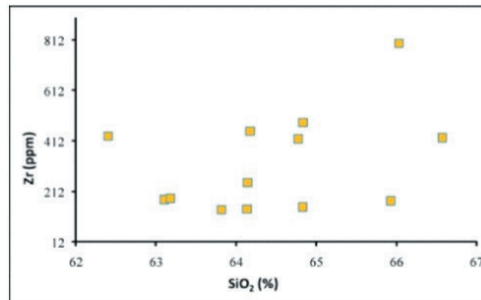

Fig. 24: Binary variation diagram of SiO$_2$ vs. Zr for the metamorphosed sandstone
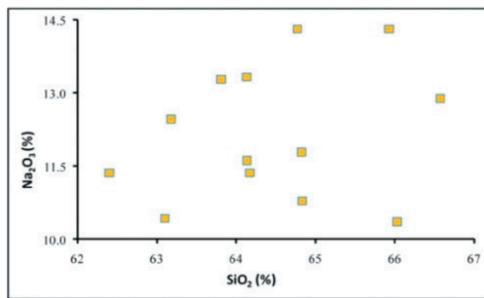

Fig. 22: Binary variation diagram of SiO$_2$ vs. Na$_2$O$_3$ for the metamorphosed sandstone
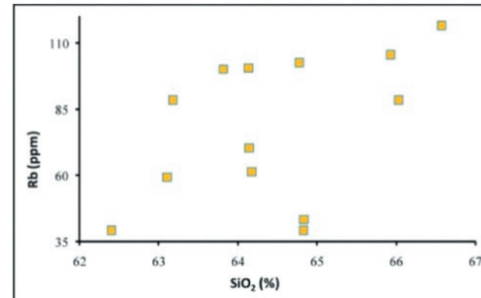

Fig. 25: Binary variation diagram of K$_2$O vs. Rb for the metamorphosed sandstone

support the low mineralogical maturity (Argest and Donnelly, 1987).

•The geochemical classification of the studied metamorphosed sandstone indicated the greywacke composition through plotting of the relevant data on binary diagrams of SiO$_2$ /Al$_2$O$_3$ vs. K$_2$O/Na$_2$O (Wimmenauer, 1984)

(Fig. 30). More verification on the paragensis and the probable source of the concerned rock was obtained using the binary diagram of SiO$_2$/Al$_2$O$_3$ versus 100 (TiO$_2$/Zr) after Haussinger et al. (1993) where approximately all the samples were plotted into or very confined to the passamatic greywacke field (Fig. 31).
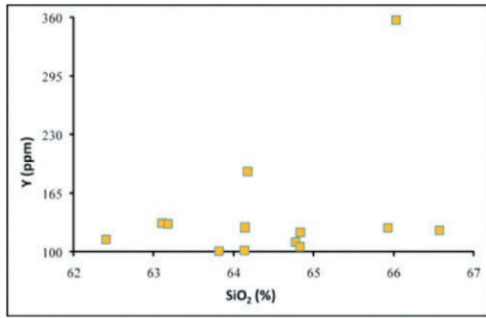
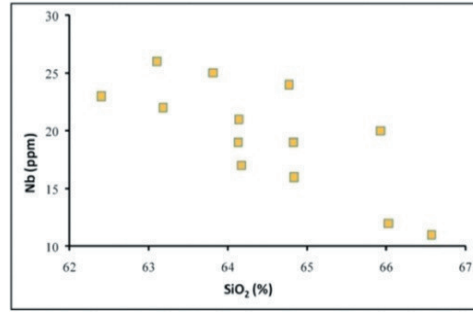Fig. 26: Binary variation diagram of SiO_2 vs. Y for the metamorphosed sandstone

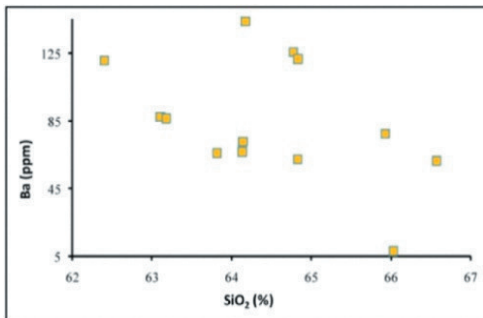Fig. 29: Binary variation diagram of SiO_2 vs. Nb for the metamorphosed sandstone

Fig. 27: Binary variation diagram of SiO_2 vs. Ba for the metamorphosed sandstone
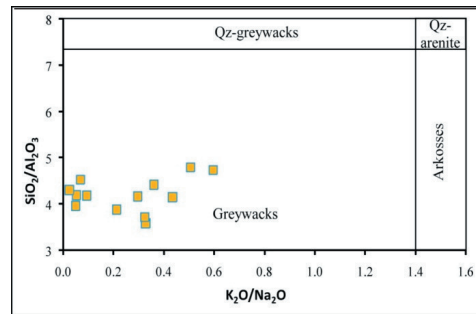
Fig. 30: Binary variation diagram of SiO_2/Al_2O_3 vs. K_2O/Na_2O after Wimmenauer (1984)
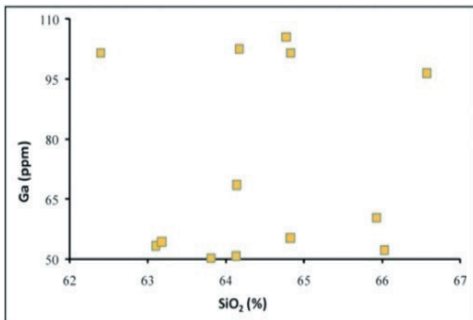
Fig. 28: Binary variation diagram of SiO_2 vs. Ga for the metamorphosed sandstone
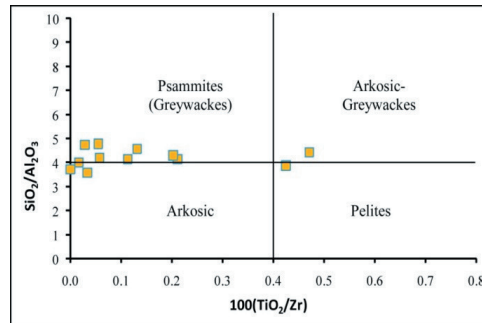
Fig. 31: Binary variation diagram of $100(TiO_2/Zr)$ vs. SiO_2/Al_2O_3 after Haussinger (1993)

• The alteration index of the metamorphosed sandstone was investigated based on the substantial variations in the concentrations of Na, Ca, Mg and Fe. Plotting of the analyzed samples on the variation diagram of Na_2O+CaO (wt%) versus $MgO+Fe_2O_3$ (wt%) after Le Maitre et al. (1989) showed the alteration was manifested by the albitization (Fig. 32).

Fig. 32: Binary variation diagram of Na_2O+CaO vs. $MgO+Fe_2O_3$ after Le Maitre et al. (1989)

Fig. 33: Binary variation diagram of SiO_2 vs. K_2O/Na_2O after Roser and Korsch (1986)

•The tectonic setting of Sikait metamorphosed sandstone was recognized using the tectonic discrimination diagram of K_2O/Na_2O versus SiO_2 (Roser & Korsch, 1986). The plotted data revealed both the island arc and the 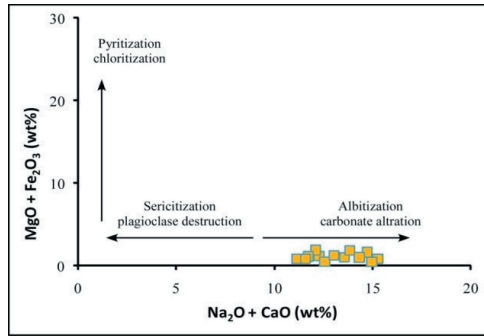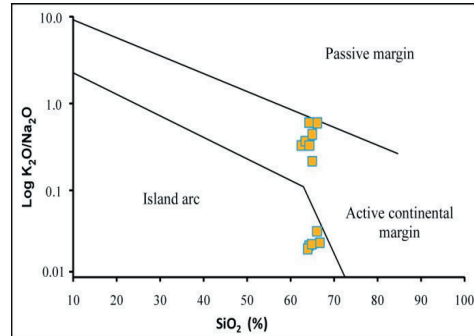active continental margin as the probable tectonic setting. Such variance may be interpreted by multiple sources of the metamorphosed sandstone and these sources were varied in their K-feldspar content (Fig. 33).

•The provenance of the studied metamorphosed sandstone was distinguished using the binary variant relation of F3 versus F4 (as function of the major components concentrations) after Roser and Korsch (1988). The plotted samples revealed the felsic igneous provenance as the primary provenance of metamorphosed sandstone (Fig. 34).
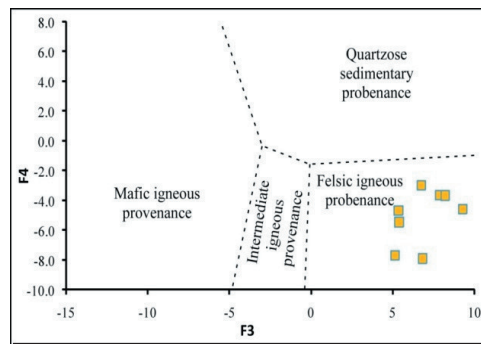
Fig. 34: Binary variation diagram for the provenance signature (After Roser and Korsch, 1988)

The Mylonite

Fourteen samples were subjected to complete chemical analysis and the achievable major and trace elements concentrations (Tables 3&4) were plotting on some discrimination diagrams to conduct the geochemical features of the concerned rock.

•The binary variation diagrams of SiO_2 against the other major oxides and trace elements (Figs. 35-43) showed the scattering realtion as the dominant one. In rocks of igneous origin, such relation suggests the source

Fig. 35: Binary variation diagram of SiO_2 vs. Al_2O_3 for the mylonite

Table 3: The major elements contents (wt%) of mylonite , Sikait area

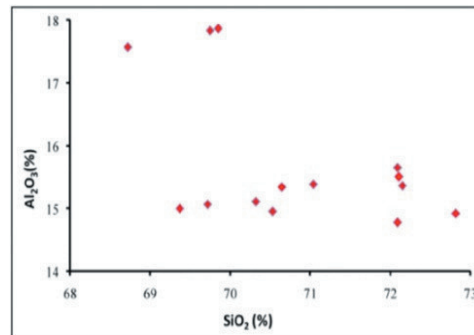| •	SiO_2	Al_2O_3	TiO_2	Fe_2O_{3t}	MgO	CaO	K_2O	Na_2O	P_2O_5	L.O.I	Total
M1	69.37	14.99	0.16	3.18	0.80	0.71	3.30	4.40	0.62	1.59	99.12
M2	72.15	15.36	0.02	0.54	0.52	0.71	3.38	5.61	0.58	1.03	99.90
M3	72.09	14.77	0.91	0.82	0.64	0.70	3.07	4.75	0.06	0.23	98.05
M4	70.53	14.95	0.01	0.53	0.12	0.52	4.86	6.14	0.62	1.54	99.82
M5	72.09	15.65	0.07	0.61	0.36	0.75	2.89	5.38	0.42	1.15	99.37
M6	72.82	14.92	0.92	0.83	0.65	0.71	3.10	4.80	0.06	0.23	99.04
M7	71.04	15.38	0.07	0.60	0.36	0.74	2.85	5.29	0.41	1.12	97.86
M8	69.85	17.86	0.06	0.55	0.60	0.71	3.02	6.68	0.46	0.24	100.03
M9	70.32	15.11	0.07	0.59	0.35	0.73	2.80	5.19	0.40	1.09	96.67
M10	69.75	17.83	0.04	0.52	0.20	0.72	2.87	6.23	0.67	2.13	100.97
M11	69.72	15.06	0.16	3.20	0.80	0.71	3.32	4.42	0.62	1.60	99.62
M12	72.11	15.50	0.04	1.79	0.05	0.62	4.72	2.46	0.57	2.70	100.56
M13	70.65	15.34	0.07	0.60	0.35	0.74	2.83	5.27	0.41	1.13	97.38
M14	68.72	17.57	0.04	0.51	0.20	0.71	2.83	6.14	0.66	2.10	99.48
Min.	68.72	14.77	0.01	0.51	0.05	0.52	2.80	2.46	0.06	0.23	96.67
Max.	72.82	17.86	0.92	3.20	0.80	0.75	4.86	6.68	0.67	2.70	100.97
Aver.	70.80	15.74	0.19	1.06	0.43	0.70	3.27	5.20	0.47	1.28	99.13

Table 4: The trace elements contents (ppm) of mylonite , Sikait area

| •	Cr	Ni	Cu	Zn	Zr	Rb	Y	Ba	Pb	Sr	Ga	V	Nb
M1	37.0	11.0	11.0	120.0	813.6	449.0	204.0	215.0	19.0	18.0	10.0	4.0	312.0
M2	24.0	7.0	11.0	14.0	432.0	405.0	112.0	38.0	9.0	9.0	7.0	U.D	168.0
M3	19.8	9.9	8.9	16.8	766.3	276.2	196.0	83.2	17.8	16.8	8.9	U.D	297.0
M4	20.0	14.0	9.0	13.0	356.4	509.0	94.0	30.0	18.0	7.0	14.0	U.D	140.0
M5	12.0	7.0	9.0	12.0	876.6	133.0	224.0	137.0	14.0	20.0	11.0	2.0	344.0
M6	20.0	10.0	9.0	17.0	774.0	279.0	198.0	84.0	18.0	17.0	9.0	U.D	300.0
M7	11.8	6.9	8.8	11.8	865.0	129.1	221.0	136.2	13.8	19.7	10.9	U.D	339.5
M8	17.0	10.0	10.0	18.0	646.2	265.0	166.0	111.0	16.0	14.0	8.0	3.0	252.0
M9	11.5	6.7	8.7	11.5	853.4	125.3	218.1	135.4	13.6	19.5	10.8	U.D	335.0
M10	16.2	9.1	11.2	16.2	772.8	257.8	197.9	54.8	13.2	17.3	7.1	U.D	300.4
M11	37.2	11.1	11.1	120.6	817.7	451.3	205.0	216.1	19.1	18.1	10.1	4.0	313.6
M12	20.0	3.0	9.0	14.0	324.0	455.0	85.0	34.0	15.0	6.0	4.0	U.D	128.0
M13	11.8	6.9	8.8	11.8	859.1	130.3	219.5	134.3	13.7	19.6	10.8	2.0	337.1
M14	16.0	9.0	11.0	16.0	761.4	254.0	195.0	54.0	13.0	17.0	7.0	U.D	296.0
Min.	11.5	3.0	8.7	11.5	324.0	125.3	85.0	30.0	9.0	6.0	4.0	U.D	128.0
Max.	37.2	14.0	11.2	120.6	876.6	509.0	224.0	216.1	19.1	20.0	14.0	4.0	344.0
Aver.	19.6	8.7	9.7	29.5	708.5	294.2	181.1	104.5	15.2	15.6	9.2	2.5	275.9
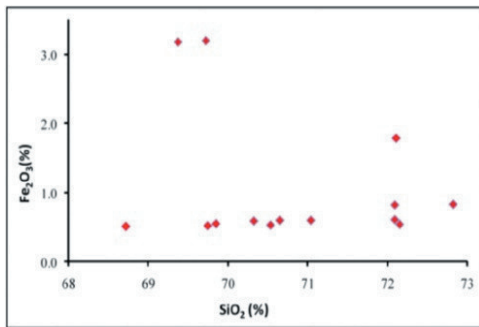
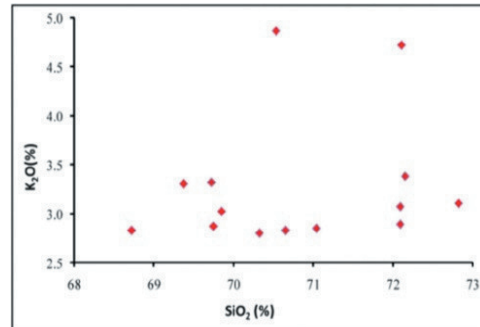Fig. 36: Binary variation diagram of SiO_2 vs. Fe_2O_3 for the mylonite

Fig. 37: Binary variation diagram of SiO_2 vs. K_2O for the mylonite

Fig. 38: Binary variation diagram of SiO$_2$ vs. Na$_2$O$_3$ for the mylonite

Fig. 41: Binary variation diagram of SiO$_2$ vs. Ba for the mylonite

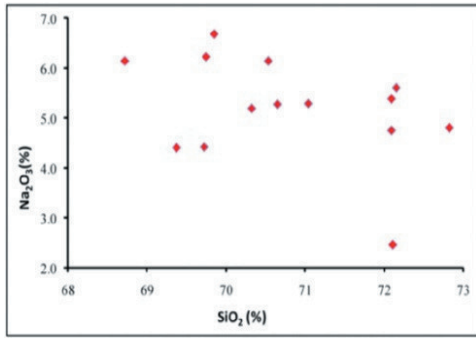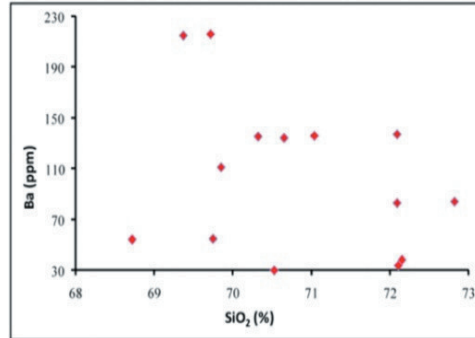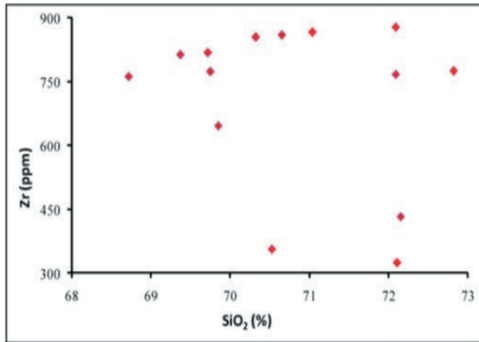Fig. 39: Binary variation diagram of SiO$_2$ vs. Zr for the mylonite
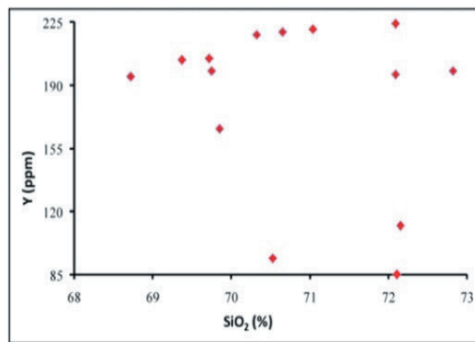

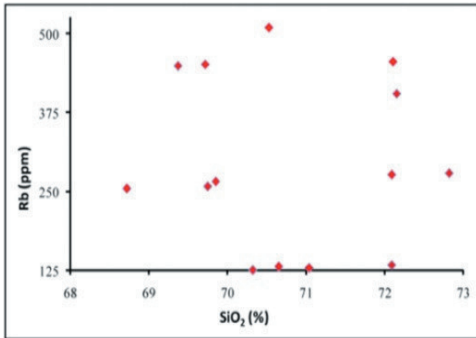Fig. 42: Binary variation diagram of SiO$_2$ vs. Y for the mylonite

Fig. 40: Binary variation diagram of SiO$_2$ vs. Rb for the mylonite
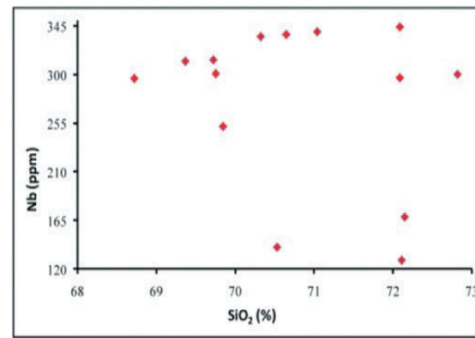

Fig. 43: Binary variation diagram of SiO$_2$ vs. Nb for the mylonite

magma was originated by assimilation and/or the partial melting (Mohammaden, 2000).

• To identify the original rock of the mylonitic samples, the binary relation between SiO_2 (wt%) versus Na_2O+K_2O (wt%) after Cox et al. (1979) was employed. The plotted samples were confined to the granite and alkali granite fields (Fig. 44).

• The magma type was tested using several discrimination diagrams; SiO_2 (wt %) - total alkalis (wt %) after Irvine and Baragar, (1971), K_2O (wt%) versus SiO_2 (wt%) after Le Maitre et al. (1989) and the ternary diagram of $Al_2O_3 – CaO - (Na_2O+K_2O)$ after Radain et al. (1982). The plotting results indicated the sub-alkaline, the medium potassic and the peraluminous nature of the source magma (Figs. 45-47).

• Furthermore, based on controlling the behaviour of LIL elements (Rb, Sr and Ba) by the major minerals (K-feldspar, plagioclase and mica), the studied samples were tested using Sr versus Rb/Sr binary diagram after Arth (1976). The plotted samples showed the consistency of their incompatible elements with the plagioclase rather than the alkali feldspars and biotite (Fig. 48). On the other hand, testing of the alteration trend based on the binary relation of Na_2O versus K_2O after Cuney et al., (1989) on which five alteration trends are defined, revealed that approximately all the samples follow the Na-metasomatism trend (Fig. 49) that matches with their consistency with plagioclase rather than the K-feldspars and biotite.

• The type of the concerned rock was accomplished using the discrimination diagram of K_2O versus Na_2O (White & Chappell, 1984 and Liew et al., 1989). The mylonitic samples are assigned as A-type (Fig. 50) which supports the anorogenic tectonic setting with probable origin from high-temperature partial melting of melt-depleted, relatively dry source (Whalen et al., 1987).

• For defining the tectonic environment of the concerned rock, the tectonic-discrimina-

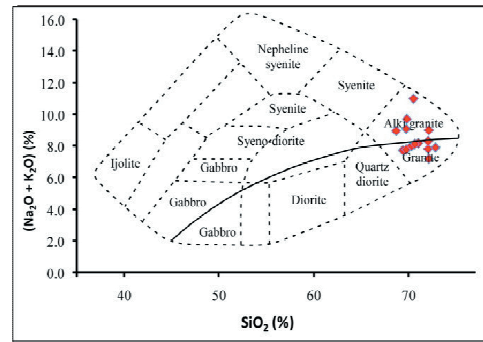Fig. 44: Binary variation diagram of SiO_2 vs. Na_2O+K_2O (After Cox et al., 1979)
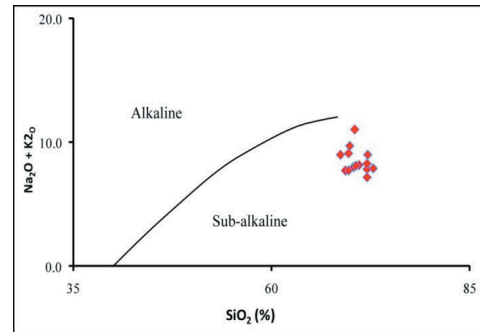

Fig. 45: Binary variation diagram of SiO_2 vs. total alkalis, (After Irvine and Baragar,1971)
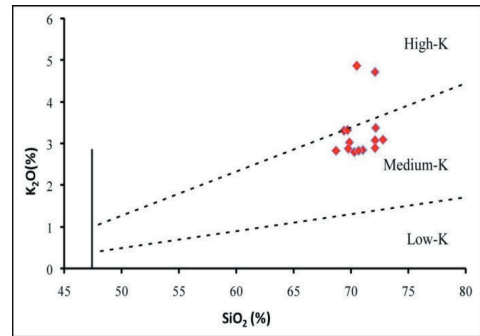

Fig. 46: Binary variation diagram of SiO_2 vs. K_2O (Le Maitre et al., 1989)
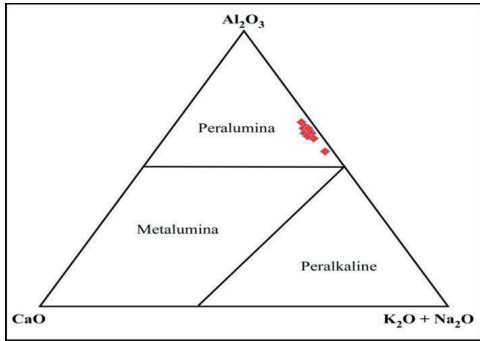
Fig. 47: Al$_2$O$_3$-CaO-(K$_2$O +Na$_2$O) ternary plot for granitic rocks (After Radain et al.,1982)
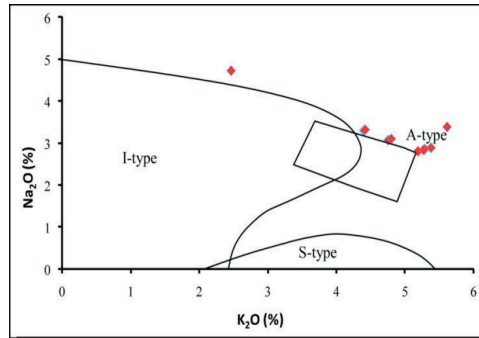
Fig. 50: Binary variation diagram of K$_2$O vs. Na$_2$O (After White and Chappel, 1984 and Liew et al.,1989)
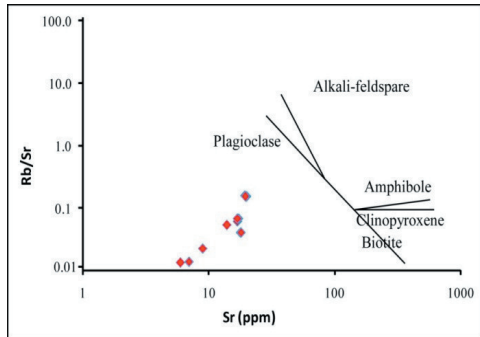
Fig. 48: Binary variation diagram of Sr vs. Rb/Sr (After Arth ,1976)
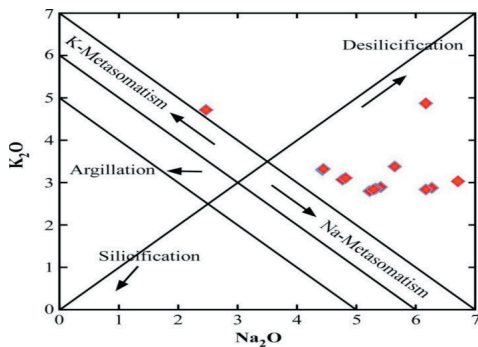
Fig. 49: Binary variation diagram of Na$_2$O vs. K$_2$O (After Cuney et al.,1989)

tion diagrams of SiO$_2$ versus Nb (Pearce and Gale, 1977) and Y+Nb versus Rb (Pearce et al., 1984) were employed. From the plotted data, the within plate environment was the suggested tectonic environment in which the granitic protolith of the mylonite was emplaced (Fig. 51).

THE RADIOMETRIC CHARACTERISTICS

Thirteen samples of the metamorphosed sandstone and fourteen samples of the mylonite were subjected to the gamma-spectrometry measurement for their concentrations of eU, eTh, Ra and K-40, additionally they also measured by wet chemistry technique to determine the chemical uranium contents. The obtained data are illustrated in Tables (5&6), also some radiometric ratios were calculated and listed in Tables (7&8).

Remarks on the Radioelements Distribution

From the data of the radiometrically measured uranium and thorium as well as the chemically measured uranium in both the metamorphosed sandstone and mylonite samples some remarks can be concluded:

-The radiometric and chemical uranium
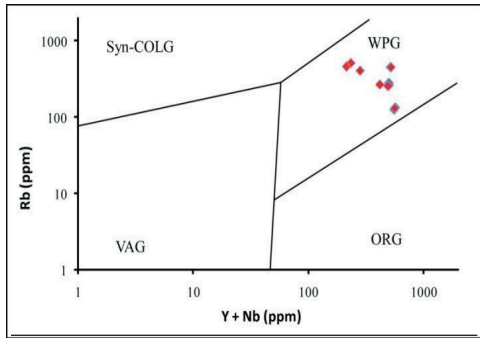
Fig. 51: Binary variation diagram of Rb vs. Y+Nb (After Pearce et al., 1984)

values in both rocks point to a significant recent uranium in the mylonite relative to the metamorphosed sandstone which might reflect a role of uranium migration to the mylonite and/or the effect of hydrothermal solution.

-Referring to the stability of thorium element and the natural ratio of U:Th (1:3.5), it can be concluded that uranium additional process impacted on both the studied rocks.

-The high content of the chemically measured uranium in the mylonite comparing to the metamorphosed sandstone appears in consistence with presence of secondary uranium minerals in the mylonite (uranophane and kasolite) while the recent uranium in the metamorphosed sandstone is probably captured by the clay matrix as elemental uranium.

**Radiometric Equilibrium in the Studied Rocks**

Equilibrium of the uranium decay series in both the rocks can be investigated as a function of some calculated radioactive ratios (Tables 5&6).

-The ratio of the radiometric measured uranium and radium (eU/Ra) is known as P-factor (Motalin, 1991 and El Galy. 1994), where departure of this ratio from unity indicates a disequilibrium state. In the studied samples, almost all of the eU/Ra ratios are out of the unity value indicating the disequilibrium in their uranium decay series (Figs. 52&53).

Table 5: Gamma-spectrometry measurements of metamorphosed sandstone and the chemically measured uranium

	eU(ppm)	eTh(ppm)	Ra (ppm)	K%	U-chem (ppm)
S1	25.87	29.85	13.93	0.00	24.88
S2	30.85	35.82	17.91	3.24	37.81
S3	18.91	27.86	10.95	4.87	22.89
S4	17.91	32.84	13.93	2.08	36.82
S5	25.87	57.71	12.94	2.59	17.91
S6	24.88	33.83	19.90	2.06	32.84
S7	14.93	33.83	16.92	2.16	19.90
S8	28.86	35.82	17.91	3.83	27.86
S9	32.84	55.72	19.90	0.07	32.84
S10	16.92	25.87	14.93	1.88	20.90
S11	21.89	32.84	16.92	2.69	29.85
S12	26.87	36.82	19.90	2.98	29.85
S13	17.91	35.82	14.93	2.80	31.84
Min.	14.93	25.87	10.95	0.00	17.91
Max.	32.84	57.71	19.90	4.87	37.81
Aver.	23.42	36.51	16.23	2.40	28.17

Table 6: Gamma-spectrometry measurements of the mylonite and the chemically measured uranium

	eU(ppm)	eTh(ppm)	Ra (ppm)	K%	U-chem. (ppm)
M1	21.00	34.00	13.00	3.30	26.00
M2	20.00	33.00	13.00	3.45	64.00
M3	28.91	18.88	20.00	3.42	60.00
M4	12.00	37.00	7.00	4.78	46.00
M5	28.00	74.00	19.00	1.56	42.00
M6	37.00	50.00	20.00	2.44	71.00
M7	27.67	73.30	18.73	1.52	40.40
M8	27.00	49.00	16.00	3.10	82.00
M9	27.33	72.60	18.45	1.47	38.80
M10	22.33	46.69	18.27	2.90	106.58
M11	21.11	34.17	13.07	3.32	26.13
M12	12.00	33.00	8.00	4.92	100.00
M13	29.05	18.97	20.10	3.44	59.00
M14	22.00	46.00	18.00	2.86	105.00
Min.	12.00	18.88	7.00	1.47	26.00
Max.	37.00	74.00	20.10	4.92	106.58
Aver.	23.96	44.33	15.90	3.03	61.92

Fig. 52: Binary variation diagram of eU vs. Ra for the metamorphosed sanstone
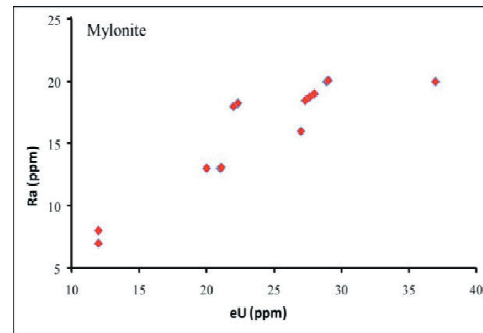
Fig.53: Binary variation diagram of eU vs. Ra for the mylonite

Dominance of the values greater than one reflects probability of recent uranium addition to the studied rocks and supports the hydrothermal mechanism of the formed secondary uranium minerals (Mohammaden, 1996).

-Also, the output of eU-eTh/3.5 is a function of the uranium mobilization. The zero result of this mathematical relation indicates no uranium mobilization since its first deposition and it is of magmatic origin while the results greater or lesser than zero reflect the uranium mobilization due to addition or removal processes respectively. Referring to the obtained results (Figs. 54&55), it can conclude that the uranium stabilization was not attained by any of the investigated rocks and the addition of uranium clearly affected the uranium concen-

Fig. 54: Binary variation diagram of eU vs. eU-(eTh/3.5) for the metamorphosed sandstone

Fig. 55: Binary variation diagram of eU vs. eU-(eTh/3.5) for the mylonite

tration. Also, the wide variation in the resultants could point to more than one cycle of the uranium mobilization or a complicated history of mutual addition and removal of uranium but the more effective was the addition activity (Badran, 2016). Anyhow, this conclusion supports the one achieved from the outputs of the eU/Ra ratios of the same samples.

-However, to confirm this conclusion the D-factor was calculated. The D-factor is the ratio of the chemically measured uranium to the radiometric measured uranium in the same samples. If this factor equals one it will mean no increasing or decreasing in the uranium content since its original deposition while values more or less than one point to addition or removal process of uranium respectively

(Hansink, 1976 and Stuckless et al., 1984). According to the calculated D-factor (Tables 7&8) and its constructed binary relation (Figs. 56&57) the following conclusions have to be considered;

•The uranium addition is the only process affected the mylonite with no signs of any removal trend and this meaning is in well concordance with the results of the corresponding eU/Ra ratios which pointed to a probable recent addition of uranium.

•Although most of the calculated D-factors in the metamorphosed sandstone indicates wide uranium addition but some ratios showed removal process. Accordingly, it can be concluded that the added uranium in some
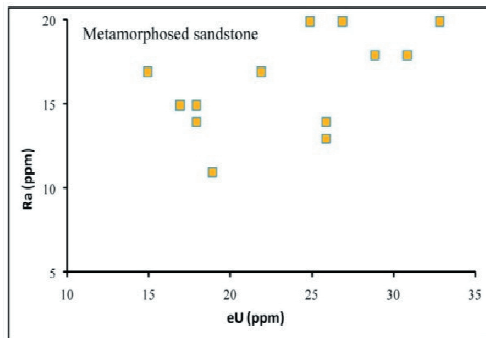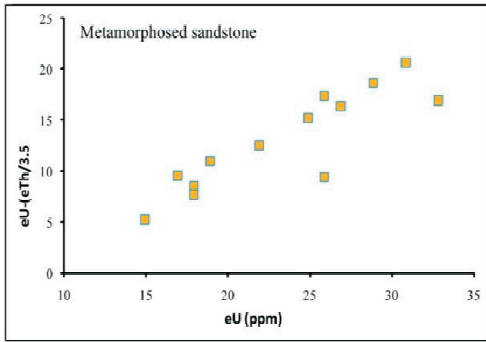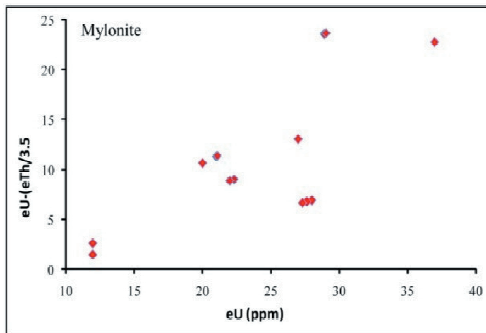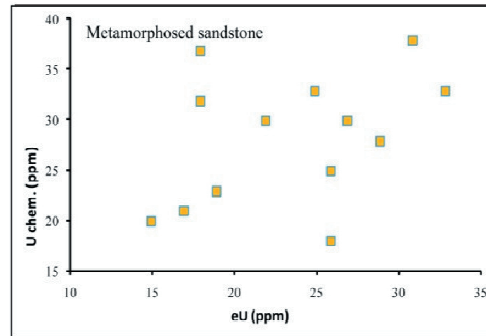

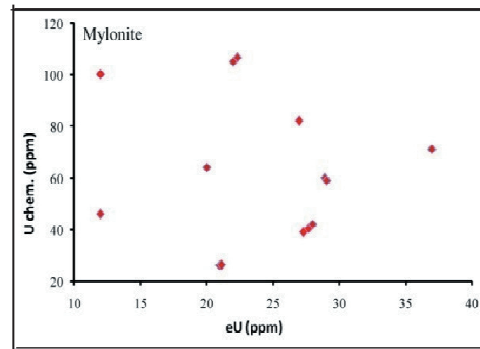Fig. 56: Binary variation diagram of eU vs. U-chem. for the metamorphosed sandstone

Fig. 57: Binary variation diagram of eU vs. U-chem. for the mylonite

MOUSTAFA E. GHARIEB et al.

Table 7: Some calculated radiometric ratios for metamorphosed sandstone

	eTh/eU	eTh/Ra	eU/eTh	eU-(eTh/3.5)	eU/Ra	U chem./U radio.
S1	1.15	2.14	0.87	17.34	1.86	0.96
S2	1.16	2.00	0.86	20.61	1.72	1.23
S3	1.47	2.55	0.68	10.95	1.73	1.21
S4	1.83	2.36	0.55	8.53	1.29	2.06
S5	2.23	4.46	0.45	9.38	2.00	0.69
S6	1.36	1.70	0.74	15.21	1.25	1.32
S7	2.27	2.00	0.44	5.26	0.88	1.33
S8	1.24	2.00	0.81	18.62	1.61	0.97
S9	1.70	2.80	0.59	16.92	1.65	1.00
S10	1.53	1.73	0.65	9.52	1.13	1.24
S11	1.50	1.94	0.67	12.51	1.29	1.36
S12	1.37	1.85	0.73	16.35	1.35	1.11
S13	2.00	2.40	0.50	7.68	1.20	1.78
Min.	1.15	1.70	0.44	5.26	0.88	0.69
Max.	2.27	4.46	0.87	20.61	2.00	2.06
Aver.	1.60	2.30	0.66	12.99	1.46	1.25

Table 8: Some calculated radiometric ratios for mylonite

	eTh/eU	eTh/Ra	eU/eTh	eU-(eTh/3.5)	eU/Ra	U chem./U radio.
M1	1.62	2.62	0.62	11.29	1.62	1.24
M2	1.65	2.54	0.61	10.57	1.54	3.20
M3	0.65	0.94	1.53	23.52	1.45	2.08
M4	3.08	5.29	0.32	1.43	1.71	3.83
M5	2.64	3.89	0.38	6.86	1.47	1.50
M6	1.35	2.50	0.74	22.71	1.85	1.92
M7	2.65	3.91	0.38	6.72	1.48	1.46
M8	1.81	3.06	0.55	13.00	1.69	3.04
M9	2.66	3.93	0.38	6.59	1.48	1.42
M10	2.09	2.56	0.48	8.99	1.22	4.77
M11	1.62	2.62	0.62	11.34	1.62	1.24
M12	2.75	4.13	0.36	2.57	1.50	8.33
M13	0.65	0.94	1.53	23.63	1.45	2.03
M14	2.09	2.56	0.48	8.86	1.22	4.77
Min.	0.65	0.94	0.32	1.43	1.22	1.24
Max.	3.08	5.29	1.53	23.63	1.85	8.33
Aver.	1.95	2.96	0.64	11.29	1.52	2.92

parts of these rocks is probably coming from other parts in the same rock, but also the uranium addition from the outside cannot be ignored.

Hosting of Th and U in the Accessory Minerals

Traditionally, the accessory minerals (particularly zircon) usually play an important role in distribution, concentration and controlling of Th and U according to the availability of these minerals in the hosting rocks.

To testify the hospitality of zircon (as the common accessory mineral in the studied rocks) toward Th and U ions, the binary relations of Zr-eTh and Zr-eU have been constructed (Figs. 58-61). The only strong correlation of Zr-eU (r = 0.84) in the mylonite and the non-significant correlation values of Zr-eTh (in mylonite), Zr-eU and Zr-eTh in the metamorphosed sandstone point to the preferentiality of uranium in the mylonite to be hosted in zircon mineral, while U in the metamorphosed sandstone and Th in both rocks behaved oppositely (Saleh et.al., 2007).

CONCLUSIONS

According to the applied studies and the achievable results some conclusions could be summarized as the following:

• The metamorphosed sandstone appeared to be originated from igneous and metamorphic sources; but also the sedimentary source could not be ignored.

• The mylonite has the characteristics of the grantitic rocks (the protolith of mylonite) that crystallized from high-differentiated magma in which the uranium element usually records elevated concentrations.

• Both the studied rocks appeared receiving recent uranium by additional process from outer source (as in mylonite) or remobilization process within the rock body (as in the metamorphosed sandstone).
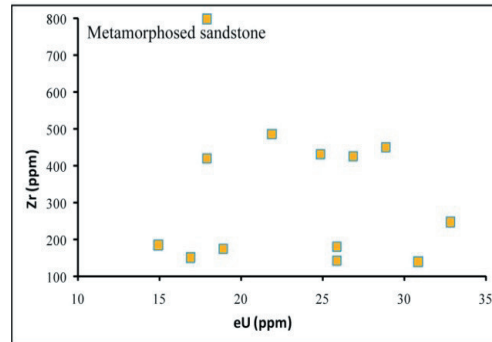

Fig. 58: Binary variation diagram of eU vs. Zr for the metamorphosed sandstone
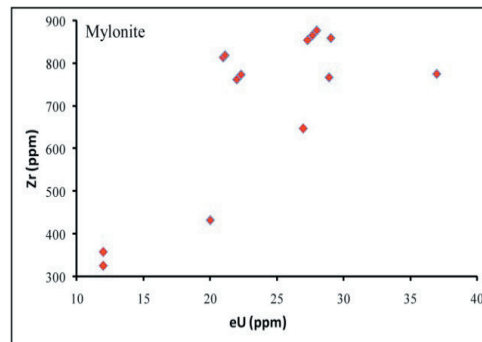

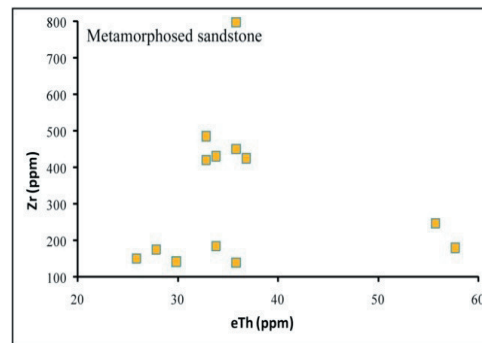Fig.59: Binary variation diagram of eU vs. Zr for the mylonite

Fig. 60: Binary variation diagram of eTh vs. Zr for the metamorphosed sandstone
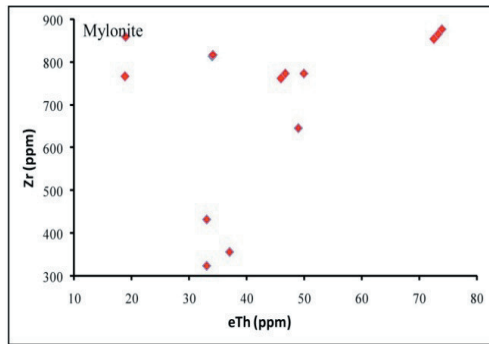
Fig. 61: Binary variation diagram of eTh vs. Zr for the mylonite

•Both the rocks are considered promising from the radioactivity point of view particularly the metamorphosed sandstone due to the easily handling of the uranium milling processes as well as the homogenous distribution of the uranium within the rock body.

•The resultants give evidences on the effect of the dynamic metamorphism rather than the thermal metamorphism and occurring of poly-phase dynamic stresses of variable magnitudes.

REFERENCES

Argest, S. and Donnelly, T.W., 1987. The chemical discrimination of clastic sedimentary components. J. Sed. Petrol, 57, 813-823.

Arth, J.G., 1976. Behavior of trace elements during magmatic processes: a summary of theoretical models and their applications. J. Res. U.S. Geol. Surv., 4, 41- 47.

Badran, M.M., 2016. Mineralogical and geochemical studies on the uranium mineralization at the contact zone between Um Greifat-Gabal Abu-Dob area, Central Eastern Desret, Egypt. Ph.D. Thesis, Suez Canal Univ., Egypt.

Cox, K.G.; Bell, J.D. and Pankhurst, R.J., 1979. The interpretation of igneous rocks. Boston, George Allen and Unwin London.

Cuney, M.; Leroy, J.; Valdiviezo, P.A.; Daziano, C.; Gamba, M.; Zarco, A.J.; Morello, O.; Nincl, C. and Molina, P., 1989. Geochemistry of the uranium mineralized Achala granitic complex Argentina: composition with Hercynian peraluminous leucogranites of Western Europe. Proceeding of Technical Committee Meeting on Metallogenesis of Uranium Deposits organized by IAEA, Vienna.

El Bayoumi, R.M. and Greiling, R.O., 1984. Tectonic evolution of Pan African plate margin in Southeastern, Egypt. A suture zone overprinted by low angle thrusting In: J. Klerkx and Michot (eds.), African Geology, Tervuren, 47-56

El-Galy, M.M., 1994. Geochemical and radiometric studies of some granitic rocks at Gabel Hamra area, South Western Sinai, Egypt. M.Sc, Thesis, Tanta Univ., Egypt.

Hansink, I.D., 1976. Equilibrium analysis of sandstone rolls front uranium deposits. Proceedings international symptosium on exploration of uranium deposits. In: Atomic Agency, Vienna, 683-693.

Hassan, M.A., 1964. Geology and petrographical studies of the radioactive minerals and rocks in Wadi Sikait-Wadi El Gemal area, Eastern Desert, U.A.R. M.Sc. Thesis, Fac. Sci., Cairo Univ., Egypt, 165.

Hassan, M.A., 1973. Geology and geochemistry of radioactive columbite-bearing psammitic gneiss of Wadi Abu Rusheid, South Eastern Desert, Egypt. Ann. Geol. Surv. Egy., 3, 206-225.

Haussinger, H.; Okrusch, M. and Scheepers, D., 1993. Geochemistry of pre-metamorphic hydrothermal alteration ofmetasedimentary rocks associated with the Gorob massive sulfide prospect, Damara Orogen, Namibia. Economic Geology, 88, 72-90.

Hegazy, H.M., 1984. Geology of Wadi El-Gemal area, Eastern Desert, Egypt. Ph.D. Thesis, Assuit Univ., Egypt, 271p.

Ibrahim, M.E.; Amer, T.E. and Saleh, G.M., 1999. New occurrence of some nuclear materials and gold mineralization at Wadi Sikait area, South

Eastern Desert, Egypt. First seminar on Nuclear Raw Materials and their technology, Cairo, Egypt, 271-284.

Ibrahim, M.E. and Ragab, A.A., 2011. Geochemistry of lamprophyre dykes, Wadi Sikait area, South Eastern Desert, Egypt. Chin. J. Geochem., 30, 323-331

Ibrahim, M.E.; Saleh, G.M.; Watanabe, K. and Ibrahim, W.S., 2015. Abu Rusheid lamprophyre dikes, South Eastern Desert, Egypt: As physical-chemical traps for REEs, Zn, Y, U, Cu, W, and Ag. Arab J. Geosci., 8, 9261-9270.

Ibrahim, M.E.; Saleh, G.M.; Hassan, M.A.; El Tookhi and Rashed M.A. 2007. Geochemistry of lamprophyres bearing uranium mineralization, Abu Rusheid area, South Eastern Desert, Egypt. The 10th Inter. Min. petrol. Metall. Engin. Conf., Assuit Univ., Egypt.

Ibrahim, M.E.; Saleh, G.M. and Ibrahim, W.S., 2010. Low grade metamorphosed sandstone-type uranium deposit, Wadi Sikait, South Eastern Desert, Egypt. J. Geol. Mining Res., 6, 129-141.

Ibrahim, W.S., Ibrahim, M.E., Watanabe, K. and Soliman, F. A. 2014. Deformation history of Nugrus-Sikiat Belt, South Eastern Desert, Egypt. Implication for tectonic environment. Intern. Res. J. Geol. Mining (IRJGM), 3, 84-100.

Irvine, T.N. and Baragar, W.A., 1971. A guide to the chemical classification of the common volcanic rocks, Canad. J. Earth Sci., 8, 523-548.

Khaleal, F.M.; Rashed, M.A. and Darwish, M.S., 2007. Base metal mineralization at Wadi Sikait, South Eastern Desert, Egypt. The 5th Inter. Conf. Geology Africa, 1, 27-39.

Khaleal, F.M., 2005. Geologic evaluation of some rare metal resources in Nugrus-sikait area, Eastern Desert, Egypt. Ph.D. Thesis, Fac. Sci., Al-Azhar Univ., Egypt.

Le Maitre, R.W.; Bateman, P.; Dudek, A.; Keiler, J.; Lameyre Le Bas, M.J.; Sabine, P.A.; Schmidt, R.; Sorensen, H.; Streckeisen, A.; Woolley, A.R. and Zanatin, B., 1989. Aclassification of Igneous Rocks and Glossary of Terms Recommendations of The International Union of Geological Sciences Subcommission on the Systematics of Igneous Rocks. Blackwell Scientific Publications, London; 193p.

Liew, T.; Finger, F., And Hock, V., 1989. The modelanubian granitoid plutonic of Astria, Chemical isotopic studies bearing their environmental setting. Chem. Geol., 46, 41-55.

Marczanko, Z., 1986. Separation and spectrophotometric determination of elements. Halsted Press. A division of John Willy and sons, New York, 677p.

Mohamed, F.H., and Hassanen, M.A., 1997. Geochemistry and petrogenesis of Sikait leucogranite, Egypt: An example of S-type granite in a metapelitic sequence. Geol. Rundsch., 86, 81-92.

Mohammaden, T.F., 1996. Correlative studies on some uraniferous radioactive granitic rock in Qattar, El-Missikat, El-Erediya and Um-Ara areas, Eastern Desert. Egypt. M.Sc. Thesis, Fac. Sci., Ain Shams Univ., Egypt, 146p.

Mohammaden, T.F., 2000. Petrographic, geochemical and isotopic characterization of granitoid rocks in Wadi Shawab area, South Wadi El-Gemal. Eastern Desert, Egypt. Ph.D. Thesis, Fac. Sci., Ain Shams Univ., Egypt, 202p.

Motalin, M., 1991. A report to the government of the Arab Republic of Egypt, Constriction and use of spectrometric calibration pads, Egypt/4/030-03, Nuclear Materials authority of Egypt.

Pearce, J.A.; Nigel, P.W. and Andrew, G.T., 1984. Trace element discrimination diagrams for the tectonic interpretation of granitic rocks. J. Petrol., 25, 956-983.

Radain, A.A.M.; Fyfe, W.S. and Kerrich, R., 1982. Origin of peralkaline granites of Saudi Arabia. Contrib Mineral. Petrol., 78, 357-366.

Ries, A.C.; Shackleton, R.M.; Graham, R.B. and Fitches, W.R., 1983. Pan-African structures,

ophiolites and mélange in the Eastern Desert of Egypt, Atraverse at 26 N, J. Geol. Soc., London, 140, 75-95.

Rogers, J.W. and Greenberg, J.K., 1981. Alkali granites and their relation to cratonization. Geol. Soc. Amer. Bull., 92 (1), 6-9.

Roser, B.P. and Korsch, R.J. 1986. Determination of tectonic setting of sandstone-mudstone suites using SiO_2 content and K_2O/Na_2O ratio. J. Geol., 94, 635-650.

Roser, B.P. and Korsch, R.J., 1988. Provenance signatures of sandstone-mudstone suites determined using discriminant function analysis of major element data. Chem. Geo., 67, 119-139.

Saleh, G.M., 1997. The potentiality of uranium occurrences in Wadi Nugrus Area, South Eastern Desert, Egypt. Ph.D. Thesis, Mansoura Univ., Egypt, 171p.

Saleh, G.M.; Azab, M.S.; Drawish, M.E.; Mansour, G.M.; Mohammaden, T.F.; Oraby, F.A.; Abu El-Hassan, E. and Rashed, M.A., 2007. Origin glate-to post-orogenic Hafafit younger granitoids, Southeastern Desert, Egypt. 10th Inter. Min. petrol. Metall. Engin. Conf., Assuit Univ., Egypt.

Saleh, G.M.; Abdallah, S.A.; Abbas, A.A.; Dawood, N.A. and Rashed, M.A., 2012. Urani-

um mineralizations of Wadi Sikait mylonites, Southeastern Desert, Egypt. J. Geol. Min. Res., 5, 86-104.

Shapiro, L., 1975. Rapid analysis of silicate, carbonate and phosphate rocks. U.S. Geol. Surv. Bull., 1401, 76p.

Stuckless, J.S.; Nkomo, I.T.; Wenner, D.B. and Van Trump, G., 1984. Geochemistry and uranium favourability of the post-orogenic granites of the northeastern Arabian Shield, Kingdome of Saudi Arabia. Bull. Fac. Earth Sci., King Abdul Aziz Univ., 6, 195-209.

Whalen, J.B.; Currie, K.I. and Chappell, B.W., 1987. A-type granites: geochemical characteristic, discrimination and petrology. Contrib. Min. Petrol., 95, 407-419.

White, A.J.R. and Chappell, B.W., 1984. Granitoids types and their distribution in the Lachlan Fold Belt. South Eastern Australia, Geol. Soc. Amer. Memo., 159, 21-34.

Wimmenauer, W., 1984. The pre Variscan crystalline basement of the Black Forest. In German. Fortschritte Mineralogie Beiheft, 62, 69-86.

Yardly, B.W., 1989. An introduction To Metamorphic Petrology, Longmann. Singapore Pub. Ltd., 248p.

———————

الخصائص الجيوكيميائية والإمكانات الإشعاعية لبعض الصخور المتحولة، وادى سيكيت، جنوب الصحراء الشرقية، مصر

مصطفى إسماعيل غريب، محمد الأحمدى إبراهيم، جمال الدين محمد عطية، سامح حمدى نجم، حسام السيد أبو المعاطى وطارق فهمى محمدين

تقع منطقة وادى سيكيت فى جنوب الصحراء الشرقيه ، مصر بين خطى عرض ١٦`` ٣٧` ٢٤ ٣٨` ـ ٢٤° شمالاً وخطى طول ٣٥``٤٦`٣٤° ـ ٣٤°٤٦``٣٥` شرقاً وتحتوى على العديد من الصخور النارية والمتحولة والتى يقطعها العديد من القواطع والعروق أهمها قواطع اللامبروفير وعروق الكوارتز. وقد تم اختيار صخرى الحجر الرملى المتحول والميولونيت لإجراء هذه الدراسه نظراً لأهميتهما من حيث المحتوى الإشعاعى.

وقد أوضحت الدراسه البتروجرافية والجيوكيميائية ان الحجر الرملى المتحول من نوع

الجرايواكى المتكون من صخور ذات أصل نارى ومتحول ومتحملة مع مشاركة محتملة من صخور رسوبية قديمة، كما تأثر هذا الصخر ببعض المحاليل الحامله للصوديوم. بينما تميز صخر الميلونيت بأصله الجرانيتى من نوع "A" ذو الصفات الكلس-قلوية و الفوق ألومينية والمتأثر أيضاً بمحاليل غنية بالصوديوم وبكونه نشأ فى بيئة "بين-الألواح التكتونيه".

هذا وقد أظهرت الدراسة الإشعاعية وقياسات اليورانيوم والثوريوم أن كلا الصخرين قد تأثرا بعمليات إضافة ليورانيوم حديث التكوين مما احدث حالة من عدم التوازن الإشعاعى فى سلسلة التحلل الإشعاعى لليورانيوم وغالباً كان اليورانيوم المُضاف هو مصدر تكوين معادن اليورانيوم الثانويه فى صخر الميلونيت بينما تم امتصاص هذا اليورانيوم فى هيئته العنصرية على حبيبات الطفلة المكونه لأرضية صخر الحجر الرملى المتحول.

وبشكل عام، فإن كلا الصخرين بصفاتهما المُتحصل عليها من الدراسة يعتبران من المصادر الواعدة لعمليات إستغلال اليورانيوم واستخراجه خاصةً صخر الحجر الرملى المتحول نظراً لسهولة إذابة اليورانيوم منه وكذلك للتوزيع المتجانس لمحتوى اليورانيوم والذى يمكن معه التقدير الجيد للمحتوى الكلى من اليورانيوم فى مُجمل الحجم والمساحة التى يشغلها فى منطقة وادى سيكيت.